Control and dissipation of runaway electron beams created during rapid shutdown experiments in DIII-D

2013 Nucl. Fusion 53 083004

(http://iopscience.iop.org/0029-5515/53/8/083004)

Nucl. Fusion **53** (2013) 083004 (15pp) doi:10.1088/0029-5515/53/8/083004

Control and dissipation of runaway electron beams created during rapid shutdown experiments in DIII-D

E.M. Hollmann[1], M.E. Austin[2], J.A. Boedo[1], N.H. Brooks[3], N. Commaux[4], N.W. Eidietis[3], D.A. Humphreys[3], V.A. Izzo[1], A.N. James[5], T.C. Jernigan[4], A. Loarte[6], J. Martin-Solis[7], R.A. Moyer[1], J.M. Muñoz-Burgos[8], P.B. Parks[3], D.L. Rudakov[1], E.J. Strait[3], C. Tsui[9], M.A. Van Zeeland[3], J.C. Wesley[3] and J.H. Yu[1]

[1] University of California-San Diego, 9500 Gilman Dr., La Jolla, CA 92093-0417, USA
[2] Institute for Fusion Studies, University of Texas at Austin, 2100 San Jacinto Blvd, Austin, TX 78712-1047, USA
[3] General Atomics, PO Box 85608, San Diego, CA 92186-5608, USA
[4] Oak Ridge National Laboratory, PO Box 2008, Oak Ridge, TX 37831, USA
[5] Lawrence Livermore National Laboratory, 7000 East Ave, Livermore, CA 94550, USA
[6] ITER Organization, Route de Vinon sur Verdon, 13115 St Paul Lez Durance, France
[7] Universidad Carlos III de Madrid, Av. Universidad 30 – 28911 Leganés, Madrid, Spain
[8] Oak Ridge Associated Universities, Oak Ridge, TN 37830, USA
[9] University of Toronto Institute for Aerospace Studies, 4925 Dufferin St, Toronto M3H 5T6, Canada

Received 25 January 2013, accepted for publication 12 June 2013
Published 3 July 2013
Online at stacks.iop.org/NF/53/083004

Abstract
DIII-D experiments on rapid shutdown runaway electron (RE) beams have improved the understanding of the processes involved in RE beam control and dissipation. Improvements in RE beam feedback control have enabled stable confinement of RE beams out to the volt-second limit of the ohmic coil, as well as enabling a ramp down to zero current. Spectroscopic studies of the RE beam have shown that neutrals tend to be excluded from the RE beam centre. Measurements of the RE energy distribution function indicate a broad distribution with mean energy of order several MeV and peak energies of order 30–40 MeV. The distribution function appears more skewed towards low energies than expected from avalanche theory. The RE pitch angle appears fairly directed ($\theta \sim 0.2$) at high energies and more isotropic at lower energies ($\varepsilon < 100$ keV). Collisional dissipation of RE beam current has been studied by massive gas injection of different impurities into RE beams; the equilibrium assimilation of these injected impurities appears to be reasonably well described by radial pressure balance between neutrals and ions. RE current dissipation following massive impurity injection is shown to be more rapid than expected from avalanche theory—this anomalous dissipation may be linked to enhanced radial diffusion caused by the significant quantity of high-Z impurities (typically argon) in the plasma. The final loss of RE beams to the wall has been studied: it was found that conversion of magnetic to kinetic energy is small for RE loss times smaller than the background plasma ohmic decay time of order 1–2 ms.

(Some figures may appear in colour only in the online journal)

1. Background

Runaway electron (RE) beams occasionally form during disruptions or rapid shutdowns in present tokamaks, and localized wall damage has occurred when these RE beams strike plasma-facing components [1]. For ITER [2], it has been predicted that a large fraction of unmitigated disruptions could lead to high current (multi-MA) RE beams [3]. This is due to the large initial plasma current ($I_p \approx 15$ MA) and large plasma size ($a \approx 1.5$ m, $R \approx 6$ m) of ITER, which are expected to lead to smaller prompt loss of RE seeds during the disruption thermal quench (TQ) [4] as well as larger RE amplification during the current quench (CQ) due to the knock-on avalanche mechanism [5]. An uncontrolled multi-MA RE beam-wall strike in ITER could lead to significant localized wall damage [6] and must therefore be avoided. A variety of research

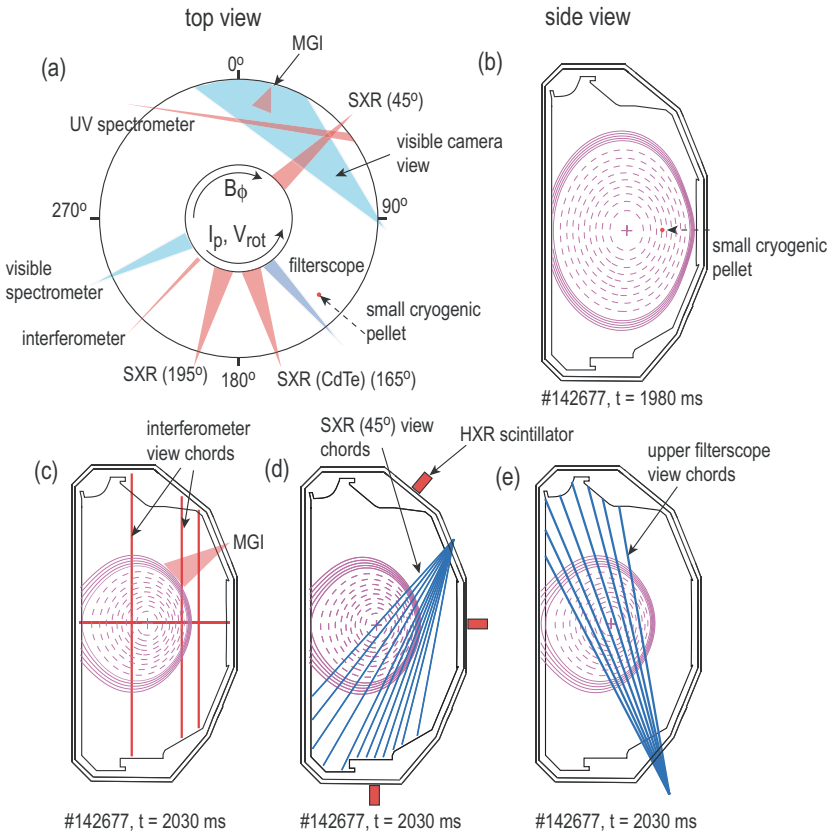

Figure 1. Overview of experimental setup showing: (*a*) top view with toroidal locations of main diagnostics, MGI nozzle and small cryogenic pellet launcher; (*b*) side view with typical target plasma shape and pellet injection poloidal location; (*c*) side view with typical RE beam plasma shape, interferometer view chords, and MGI nozzle poloidal location; (*d*) side view with HXR scintillator poloidal locations and SXR view chords; and (*e*) side view with visible spectrometer and filterscope view chords.

has been performed on avoiding performance barriers which lead to disruptions, predicting the onset of disruptions, and mitigating unavoidable disruptions in a manner which reduces RE formation, either through applied magnetic field errors or through rapid shutdown with massive particle injection [7]. Despite progress in these areas, it is thought at present that disruptions will still occur in some ITER shots and that a RE beam will form in some of these disruptions, even mitigated disruptions. It is therefore important for ITER to have in place a system to dissipate a disruption RE beam as harmlessly as possible, should one occur.

At this time, it is not certain if the ITER control system will be able to control the position of the RE beam current, since the spatial structure of RE current seeds and the subsequent evolution of RE current are not well known. Present simulations indicate that post-disruption RE beams will drift vertically in ITER, but that this vertical motion can be brought under control by the ITER control system for sufficiently well-centred or sufficiently large RE beams ($I_p > 10$ MA) [8]. However, since uncontrolled RE beam-wall strikes with currents >2 MA are thought to be potentially intolerable in ITER [9], a method for harmlessly dissipating the RE current in the regime 2 MA $< I_p <$ 10 MA needs to be developed. One potential method for doing this is massive gas injection (MGI) of high-Z gas into the RE beam [10], which is studied in this paper.

The upper bound of 2 MA allowed in ITER for a RE beam-wall strike is based on JET data [11] and assumes a RE strike wetted area similar to seen in JET IR camera images and a 40% conversion of magnetic energy to kinetic energy in the strike [9]. Data are presented here which indicate that conversion of magnetic to kinetic energy to RE-wall strikes could be less than 40% for sufficiently rapid final wall strikes. If the 2 MA upper bound could be relaxed, even to 4 MA, for example, this would relax the requirements for RE dissipation in ITER. However, significant RE damage has been seen in present machines for RE currents less than even 1 MA, so it is important to reduce RE current as much as possible in ITER.

2. Introduction to experiments

The experiments described here are performed in the DIII-D tokamak [12]. In each experiment, an initially stable discharge is shut down (usually at time $t = 2000$ ms) with rapid injection of argon; either via fast ($v \approx 500$ m s^{-1}) injection of a single small ($D \approx 2.7$ mm, 7 Torr^{-1}) solid argon pellet, or via MGI of around 1000 Torr^{-1} of argon gas. In most cases, low elongation ($\kappa \approx 1.3$–1.4), inner wall-limited (IWL), electron cyclotron heated (ECH) target plasmas are used, as these, together with rapid argon deposition, are found to be best for reliably producing large ($I_p \approx$ 200–400 kA) RE beams. Schematics of argon pellet injector and MGI nozzle locations, as well as locations of some key diagnostics, are shown in figure 1.

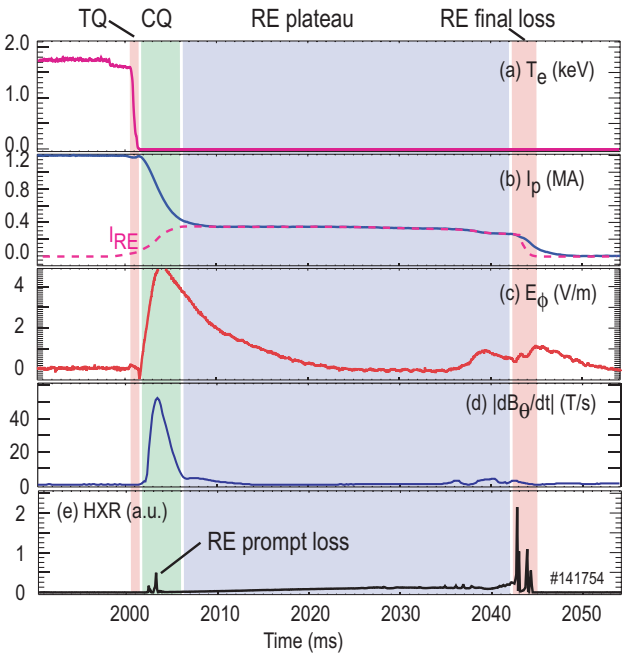

Figure 2. Overview of disruption time scales showing (*a*) central electron temperature, (*b*) plasma current, (*c*) toroidal electric field (from loop external to the vacuum vessel), (*d*) amplitude of magnetic fluctuations and (*e*) HXR signals vesrsus time. RE current in (*b*) is conceptual only.

An overview of typical experiment time scales is shown in figure 2. At $t = 2000$ ms, rapid argon injection occurs resulting in a fast (∼1 ms duration) TQ or loss of initial plasma thermal energy, figure 2(*a*). RE seeds are thought to form during the TQ phase. At the end of the TQ, some fraction of these RE seeds are lost to the wall in a RE prompt loss, seen as a flash on hard x-ray (HXR) scintillators, figure 2(*e*). Subsequently, a slower (∼4 ms duration) ohmic CQ occurs during which the plasma thermal current decays resistively. The large toroidal electric field of the CQ, figure 2(*c*), amplifies the RE current. If the RE current becomes larger than the ohmic current at that time (not the initial ohmic current), the plasma enters the RE plateau phase, where the plasma current is dominantly carried by REs. The resulting RE beam tends to drift into the wall. As this occurs, a small rise in HXR signals and loop voltage is typically observed as RE loss to the wall increases. Finally, a series of rapid large HXR bursts are observed, figure 2(*e*), probably due to some form of magnetohydrodynamic (MHD) instability, which typically results in a rapid (∼1 ms duration) final loss of REs into the wall. Some degree of magnetic activity, figure 2(*d*), is seen during both the CQ and the RE final loss. This final loss of REs into the wall is the phase which is most dangerous for ITER, and the experiments discussed here ultimately have the goal of reducing the kinetic energy released into the wall by REs during this phase. In this paper, the primary focus will be on the RE plateau and final loss phases. RE seed formation and CQ amplification, while important, will not be studied here.

Several types of experiments have been done on RE beams, roughly categorized as: (*a*) experiments where a RE plateau is created with Ar pellet injection and is then manipulated with magnetic feedback control, (*b*) experiments

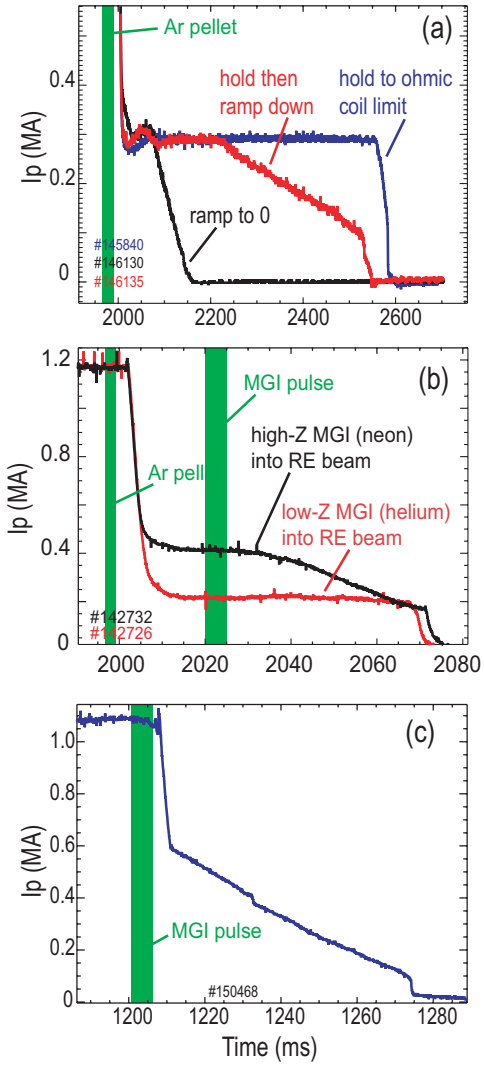

Figure 3. Plasma current versus time for different types of RE plateau experiments: (*a*) RE current control showing: shot with constant current out to Ohmic coil limit, shot held for 200 ms then ramped down, and shot immediately ramped down to zero current; (*b*) MGI-into-RE beam experiments showing enhanced decay rate following high-‘ MGI; and (*c*) RE created from argon MGI experiment where a rapid ramp down to nearly 0 current is obtained.

where a RE plateau is created with Ar pellet injection and then dissipated using MGI, and (*c*) experiments where Ar MGI is used to create the RE beam. Sample current traces versus time of these different types of experiments are shown in figures 3(*a*)–(*c*). In all the experiments, high-Z impurities (Ar) play a central role: rapid shutdown with Ar injection into hot plasmas is found to greatly enhance RE seed formation, but later the presence of the same Ar in the RE plateau also appears to enhance RE dissipation.

In the RE control experiments, RE plateaus are created with Ar pellet shutdown, creating a RE beam with a minority (∼10%) argon content. It was initially found that the RE beam tended to limit against the centre post and then drift vertically to be lost in an uncontrolled fashion against the upper or lower divertor. To prevent this RE loss, an open loop outward push from the plasma shaping coils was used to avoid erratic feedback and avoid loss of the RE beam

into the centre post. Subsequently, robust linear position estimators were implemented to enable vertical control of the RE beam position. With vertical position control of the RE beam established, ohmic feedback control of the RE beam was demonstrated, as shown in figure 3(*a*), where different RE beams are either held at constant current for 600 ms (blue), or held for 200 ms and then ramped down (red), or immediately ramped to nearly zero current (black) [13].

In the MGI-into-RE experiments, Ar pellet injection and control system feedback is used to create a vertically stable, current-controlled RE beam as described above. This stable RE beam is then perturbed with MGI (typically 300 to 1000 Torr^{-1} of either a high-Z gas such as neon or argon, or a low-Z gas such as helium). Ohmic coil current feedback is left on, so the control system attempts to maintain constant plasma current during these experiments. An enhanced RE current dissipation rate (despite the efforts of the ohmic coil to maintain constant current) is observed following high-Z injection, as seen in figure 3(*b*). Typically, a rapid (~20 ms timescale) decay of RE current is observed down to some minimum current of order 50–200 kA, at which point the RE beam is lost to the inner wall in the final loss phase. For low-Z injection, either no change or even a slightly reduced decay rate is observed; this is believed to be due to a purging of argon out of the RE beam by the injected low-Z gas.

Finally, some experiments were performed where argon MGI was used to create the initial RE plateau. The initial target plasma is similar to the above experiments. However, in these experiments, the RE beam begins with a majority (>50%) argon content, resulting in an immediate, rapid decay towards zero of the RE current. Decay of the RE current to nearly zero before final loss onset has been achieved, as shown in figure 3(*c*).

In ITER, it is anticipated that some combination of RE beam control and dissipation will be used in the event of RE beam formation. Ideally, the RE beam can be held stable vertically and then some high-Z gas can be injected to dissipate the RE current *in situ*. If the RE beam cannot be stabilized and is drifting vertically, it may still be desirable to inject some high-Z gas to increase the decay rate of the RE beam current before it strikes the wall. Minimizing RE final loss damage in this scenario will be complicated because increasing RE current decay is expected to lead to a further increased vertical loss rate, so high-Z MGI may work against itself by reducing the amount of time available for RE current dissipation. Conversely, a rapid motion of the RE beam into the wall may actually be desirable to reduce the amount of magnetic energy converted into kinetic energy during the final loss, as discussed in section 5 of this paper. Optimizing the ITER RE plateau mitigation procedure will therefore require not only modelling of the ITER control system, but understanding of RE beam structure, assimilation of injected particles into the RE beam, effect of the injected particles on RE current and energy, and damage done by RE beams to the wall as a function of their energy, current, and loss rate.

In this paper, we present measurements of the RE beam structure, composition, and energy spectrum for RE plateaus with minority argon content (section 3). Data on the assimilation of additional impurities injected into RE beams is presented, as well as data on the resulting effect on RE beam current dissipation (section 4). Finally, data on RE beam final loss characteristics is discussed (section 5).

3. Structure and composition of RE plateau

As discussed in the introduction, RE beams are typically created by rapid Ar pellet injection, resulting in a RE plateau with a minority (~10%) argon content. In this section, we present studies of the structure and composition of these RE plateaus. Section 3.1 shows that the hot ($\varepsilon > 1$ keV) electrons (REs) are dominantly found in a narrow ($a \sim 0.2$–0.3 m) beam, but are contained in a broader ($a \sim 0.5$ m) cold ($T \sim 1.5$–2.0 eV) electron plasma. Section 3.2 shows that the RE current is also found in a narrow (0.2–0.3 m) beam, consistent with the plasma current being carried dominantly by hot electrons. Section 3.3 show measurements that support that the plasma in the RE beam consists of mostly D^+ ions and a minority (~5–10%) Ar^+ ions, with neutral particles largely excluded from the RE beam. Section 3.4 presents measurements of the RE energy distribution function, and section 3.5 presents data on the RE plateau current dissipation rate.

3.1. Radial profile of hot and cold electrons

Previous work has shown that the total electron density in the RE plateau consists of two components: a cold, dense background plasma and a hot, low-density RE beam component [14]. The line-integrated cold background plasma electron density can be measured with CO_2 interferometers, and the line-integrated soft x-ray (SXR) emissivity (which qualitatively represents fast electron density, as discussed later) can be estimated from SXR view chords. The ratio of RE number to cold electron number appears to be quite small, of order 10^{-2}–10^{-3}. By using shots with rapid vertical loss and assuming that the RE beam profile does not change significantly until the onset of the final loss phase, tomographic inversions of cold electron and SXR emissivity profiles can be made. Figure 4 shows such an inversion done with SXR view chords and figure 5 shows a similar shot with such an inversion done with interferometer view chords. In figure 4, (*a*) shows the plasma current, (*b*) the vertical position, and (*c*) the HXR signals as a function of time. At time $t \approx 2053$ ms, vertical control is lost and the RE beam drifts down rapidly. As can be seen in the HXR signals, significant RE loss to the walls does not begin until $t \approx 2055$ ms. The time period $t \approx 2053$–2054.5 ms is therefore used to invert the SXR emissivity of the RE beam, assuming the beam drifts vertically over these times but does not change shape. Figure 4(*d*) shows SXR view chords and magnetic flux surface reconstructions during downward motion. The flux surfaces are calculated with a discrete current element inversion code (JFIT) constrained by external magnetic sensors [15]. Figure 4(*e*) shows measured SXR brightness versus channel number for three different time steps, as well as back-constructed SXR brightness from the inversion, showing a reasonably good fit. Figure 4(*f*) shows SXR emissivity contours and JFIT contours. Typically, we find that the SXR centre and the JFIT centre are within <10 cm of each other. Figures 5(*a*)–(*c*) show time sequences for a similar shot but with good interferometer data. Figures 5(*d*)–(*f*) show

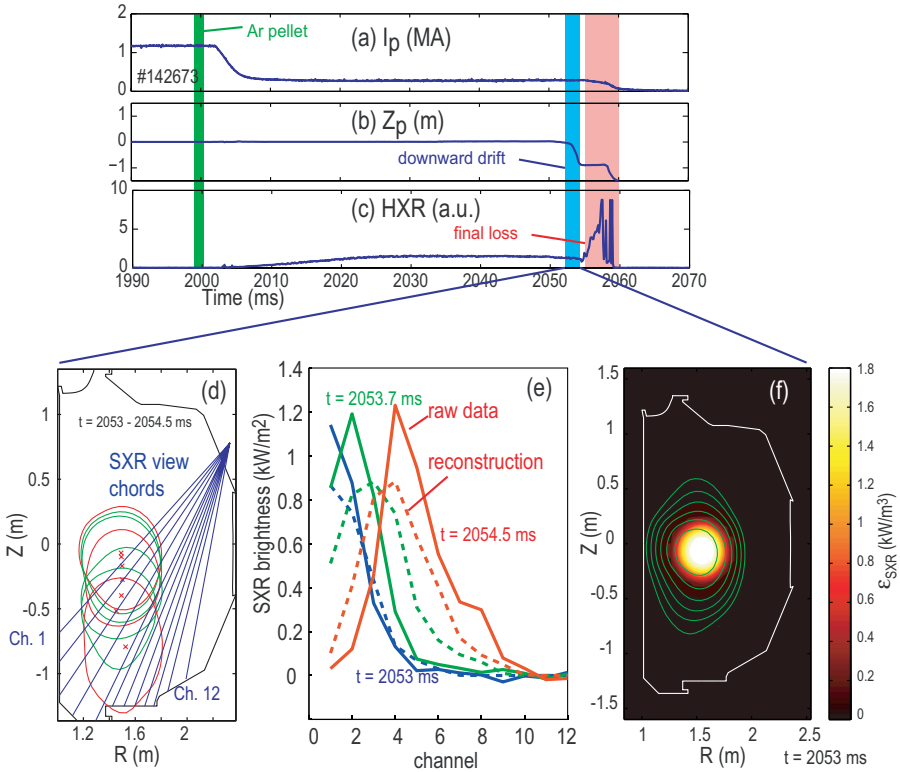

Figure 4. SXR inversion on downward moving RE beam showing: time traces of (*a*) plasma current, (*b*) plasma vertical position, and (*c*) HXR signals; then (*d*) JFIT reconstructions of flux surfaces of downward moving RE beam, (*e*) SXR brightness versus array channel number at different time steps, and (*f*) reconstructed SXR emissivity and JFIT flux surfaces.

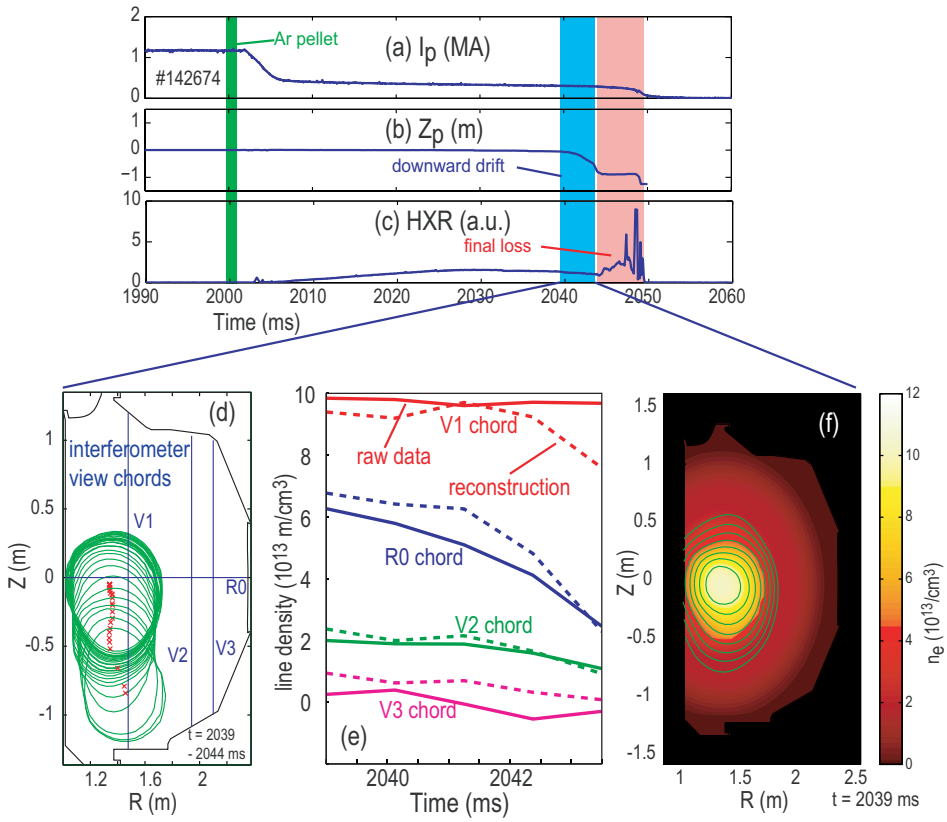

Figure 5. Interferometer inversion on downward moving RE beam showing: time traces of (*a*) plasma current, (*b*) plasma vertical position and (*c*) HXR signals; then (*d*) JFIT reconstructions of flux surfaces, (*e*) line-integrated data versus time and (*f*) reconstructed cold electron density contours and JFIT flux surfaces.

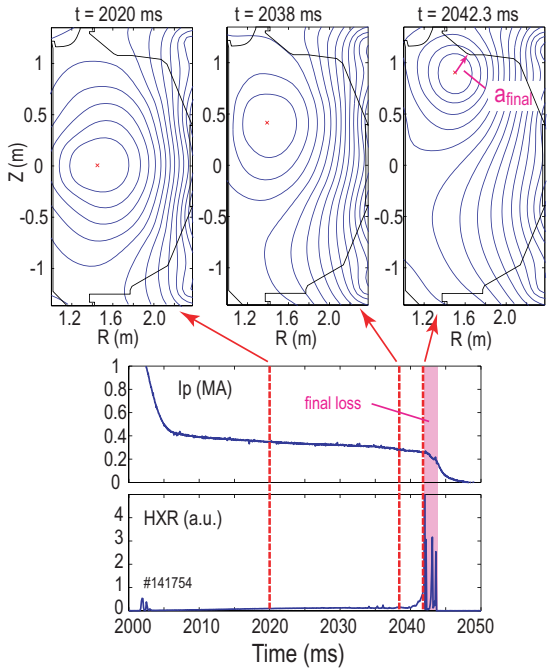

Figure 6. Illustration of method used to calculate RE beam current radius a_{final}.

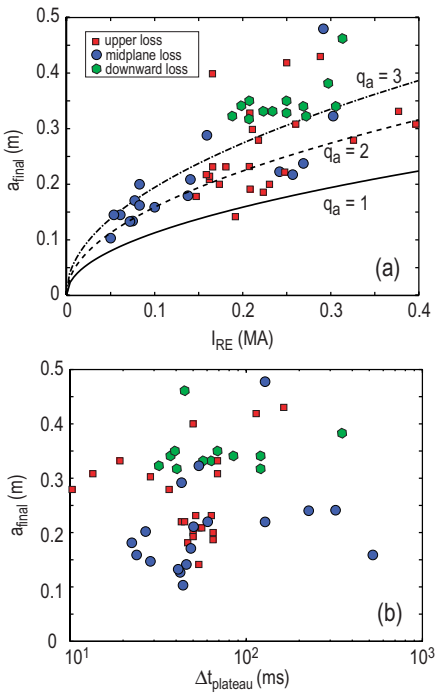

Figure 7. (*a*) Final loss radius a_{final} as a function of final loss current I_{RE} and (*b*) final loss radius as a function of duration of RE plateau $\Delta t_{\text{plateau}}$.

the reconstructed cold electron density profile; it can be seen that the cold electron profile (figure 5(*f*)) is much broader than the hot electron density profile (figure 4(*f*)). The shots shown for SXR and interferometers are different, but the results shown are fairly general, i.e. that the hot electron profile is significantly narrower than the cold electron profile. The cold plasma outside of the narrower RE beam could be sustained either by diffusion of cold plasma from the core to the wall or by ionization from REs which diffuse out of the hot core to the wall.

3.2. Current profile of RE plateau

Previous work estimated the radius of the RE beam current profile in DIII-D to be $a \approx 0.3$ m by looking at the onset time of the final loss loop voltage spike for inward-moving RE beams [13]. Here, we extend this analysis to a large number of shots, with loss directions inwards to the centre post, upwards, or downwards. Also, instead of using the rise of the externally measured loop voltage as an indicator for the onset of the final loss, the edge of the first HXR spikes is used, as this provides a sharper time step. An overview of the general method is shown in figure 6: JFIT contours are used to calculate the position of the RE beam current magnetic axis versus time; the final loss onset time is taken as the time where the large HXR spikes begin; and then the RE beam current radius a_{final} is taken as the distance between the magnetic axis and the nearest wall point at the final loss onset time.

Figure 7(*a*) shows the RE current radius a_{final} as a function of the RE current I_{RE} at the final loss time. It can be seen that there is a large range of a_{final}, but typical values are around 0.2–0.4 m, consistent with the previous estimate $a \sim 0.3$ m for the RE beam current radius, and also consistent with the measured radii of the SXR emissivity spot, $a \sim 0.2$–0.3 m, in agreement with the expectation that the hot electrons are the dominant carriers of plasma current in the RE plateau. It is not clear at this point why the RE current does not fill the entire area up to the last closed flux surface. Some REs do exist all the way out to the wall, as has been confirmed by plunging probe and pellet injection experiments, but the bulk of the current appears to form a relatively narrow beam. The increasing trend in a_{final} with I_{RE} may indicate that the onset of HXR spikes in the RE final loss is associated with a kink mode, consistent with the strong $n = 1$ structure often seen in RE final loss toroidal HXR emission structure [16]. Simple (cylindrical plasma, large aspect ratio) estimates of the expected final loss radius assuming the final loss begins at a specific edge safety factor ($q_a = 1, 2$ or 3) are shown by the curves in figure 7(*a*). It can be seen that the final loss radius may be consistent with the RE beam $q_a = 2$ edge contacting the wall, although the large scatter in the data does not allow a clear conclusion at present. For example, it could be the case that RE equilibrium beam radius simply increases as the square root of plasma current, which would give a curve similar to that shown in figure 7(*a*), without invoking any MHD. Midplane loss cases appear to show less scatter than upper and lower loss cases, possibly indicating that the JFIT reconstructions are more accurate for loss to the midplane. Relativistic shifts of RE orbits are not considered in this analysis, (although their effect on the current channel position, if significant, should be captured by the JFIT reconstructions); however, outward shifts could influence the final loss and thus give midplane versus upper and lower final loss cases different characteristics. Figure 7(*b*) shows a_{final} as a function of the duration of the RE plateau. It can be seen that there is no clear trend in RE beam radius with RE beam lifetime, indicating that slow wall time or recycling effects are not important in determining RE beam radius.

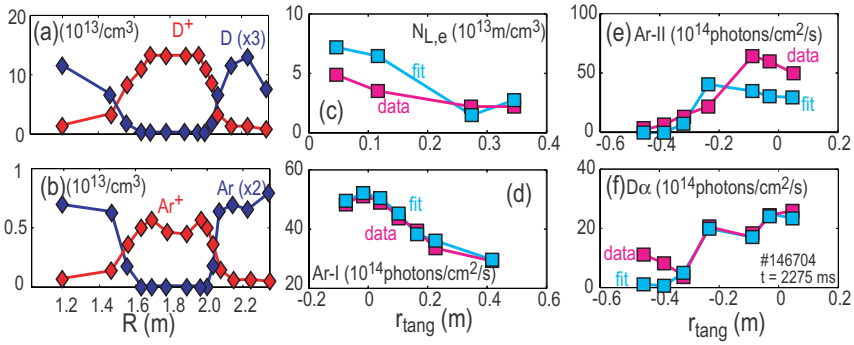

Figure 8. Midplane density profiles at $t = 2275$ ms for (a) deuterium neutrals and ions and (b) argon neutrals and ions as a function of midplane radius. (c)–(f) show quality of fits to line-integrated electron density and line brightnesses. r_{tang} is distance of closest approach of view chord to magnetic axis, with negative values indicating view chord passes between magnetic axis and centre post. Emission profiles are assumed to be flux functions.

3.3. Ion composition of RE plateau

Knowing the neutral and ion composition of the RE plateau is important for understanding its current dissipation. Tangential visible camera images suggest that visible line emissivity is a reasonably good flux function [14]. If we use JFIT contours as line emissivity contours, it is possible to use line-integrated visible line brightness data from stationary RE plateaus to make estimates of the ion and neutral densities in the RE beam. Deuterium density can be estimated from D_α (656.2 nm) brightness, Ar^+ density from Ar II (465.8 nm) brightness, Ar density from Ar I (811.5 nm) brightness, and C^+ density from C II (657.8 nm) brightness. Upward-viewing poloidal view fans are used for Ar I, Ar II, and D_α; while a tangential fan is used for C II brightness. Photon emission coefficients from ADAS [17] are used. The D^+ density can then be estimated from quasi-neutrality using the interferometer data. Figure 8 shows the resulting profiles for (a) D and D^+ and (b) Ar and Ar^+. The quality of the reconstructed line-integrated data is shown in panes (c) for interferometer data, (d) for Ar I brightness, (e) for Ar II brightness, and (f) for D_α brightness. Due to the small radial shift observed in the SXR inversions (e.g. figure 4), the inversions allow for a small (<10 cm) radial shift of the flux function contours to allow the best possible fit. Overall, it can be seen that the data is fit within a factor of two or better across the plasma profile. The relative quality of the different fits depends on the relative weights assigned to the different errors, i.e. line density fits can be improved, but at the expense of argon brightness fits. Neutrals are seen to be mostly excluded from the RE beam core, i.e. are ionized if they attempt to enter the RE beam. C^+ density, not shown here, is found to be small ($\sim$1%) in the RE beam core. Argon ion content is found to be about 5–10% in the RE beam core. Compared with the initial amount of argon in the injected pellet (2.3×10^{20} argon atoms), only 5–10% of the injected argon appears accounted for in the RE beam; the bulk of the argon apparently remains as neutrals outside the RE beam.

Line trapping is not expected to affect the results of figure 8. The lines used are not from the ground state, and therefore, are not expected to be trapped. Corresponding neutral resonance lines (e.g. Ly-α) are probably at least partially trapped and could therefore broaden the observed neutral line profile (e.g. Hα) somewhat. However, since

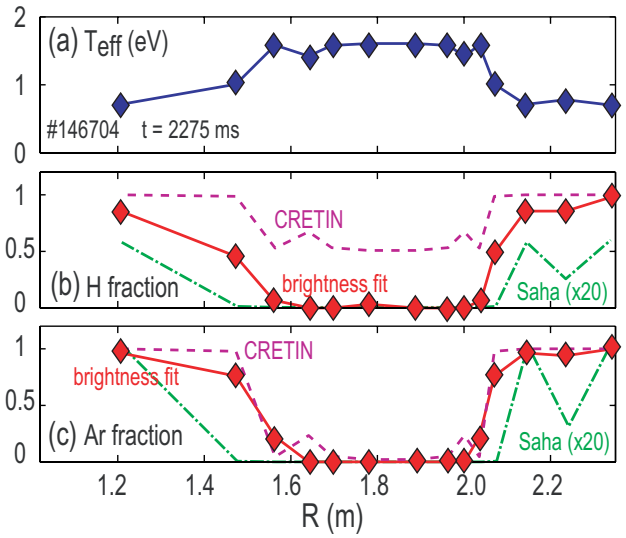

Figure 9. Radial profiles of (a) effective temperature from line brightness fit, (b) H fraction from brightness fit as well as H fraction from equilibrium calculations and (c) Ar fraction from brightness fit as well as Ar fraction from equilibrium calculations.

significant spatial structure is seen in the neutral line emission, this second-order effect is probably weak.

For the fits shown in figures 8(c)–(f), the radial profile of the effective electron temperature T_{eff} is varied as a free parameter. A central electron temperature of about 1.5 eV and edge temperature of about 0.8 eV are obtained, as shown in figure 9(a). As a rough self-consistency check, the neutral fraction obtained with the line brightness profile fits, figure 8, can be compared with the neutral fraction calculated by using the T_{eff}, measured cold electron density, and assuming ionization–recombination equilibrium. The resulting equilibrium neutral fractions for H and Ar are shown in figures 9(b) and (c) as dashed lines. It can be seen that significant hollowing of the neutral profile is predicted, in qualitative agreement with the brightness fits. Two different models are shown: CRETIN ionization–recombination equilibrium [18], which is reasonably close to the brightness fit data, and Saha equilibrium, which predicts a much lower neutral fraction.

Neutral and ion line emission appears to be caused dominantly by cold background electron impact rather than

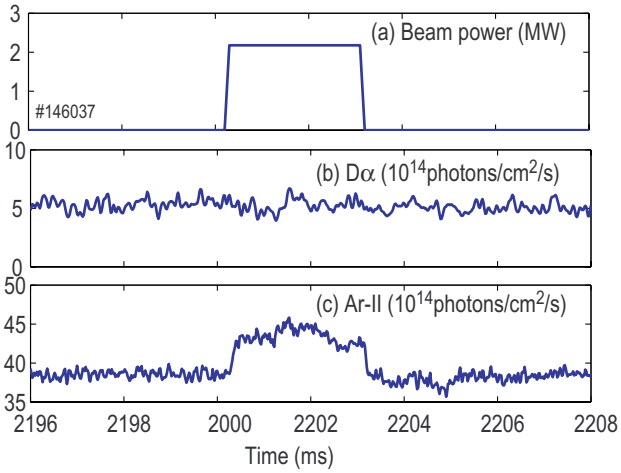

Figure 10. RE plateau line brightness measurements versus time taken during beam blip showing (*a*) beam power, (*b*) Dα brightness, and (*c*) Ar-II brightness (from the same central view chord).

hot (runaway) electron impact. Previous high-resolution spectrometer measurements of ion and neutral Doppler broadening obtained approximate temperatures $T_i \approx 1.6\,\mathrm{eV}$ for ions and $T_N \approx 1.2\,\mathrm{eV}$ for neutrals [14]. Due to the high density and low temperature of the cold electrons, it is expected that the cold electrons and plasma ions are near thermal equilibrium, thus indicating a central cold electron temperature $T_e \approx T_i \approx 1.6\,\mathrm{eV}$. Since this is similar to the central T_{eff}, the data suggests that the visible line emission is dominated by cold electron collisions, not hot electron collisions (which would presumably give some higher T_{eff}). This was supported by firing neutral beam injection (NBI) pulses into RE beams: NBI is expected to heat the cold ions (and as a consequence the cold electrons), but not the hot electrons. NBI pulses were seen to cause pulses of increased ion line emission, figure 10(*c*), consistent with line emission coming from cold electrons. Little or no effect was seen in neutral line emission, figure 10(*b*), consistent with the bulk of the neutrals being separated from the bulk of the ions.

3.4. RE energy measurements

The RE energy distribution function $f_{\mathrm{RE}}(\varepsilon)$ is important, as it affects the RE current profile, RE dissipation, and RE-wall interaction. An estimate of $f_{\mathrm{RE}}(\varepsilon)$ can be assembled from different diagnostics, each dominantly sensitive to photons in a different energy range: Si SXR detectors (mostly sensitive to photons in the 2–10 keV range); CdTe SXR detectors (mostly sensitive to photons in the 2–150 keV range), BGO HXR detectors (mostly sensitive to photons in the 1–20 MeV range), and a survey spectrometer measuring near-IR photons. SXR and HXR continuum emission is expected to be dominated by bremsstrahlung from fast electrons striking argon nuclei, while forward-beamed continuum emission in the near IR range is expected to be dominated by synchrotron emission from fast electrons, if sufficient quantities of extremely energetic ($\varepsilon > 30\,\mathrm{MeV}$) electrons are present. The approximate expected sensitivity of the different detectors to different fast electron energies are shown in figure 11. The sensitivities in figure 11 are convolved with an actual energy

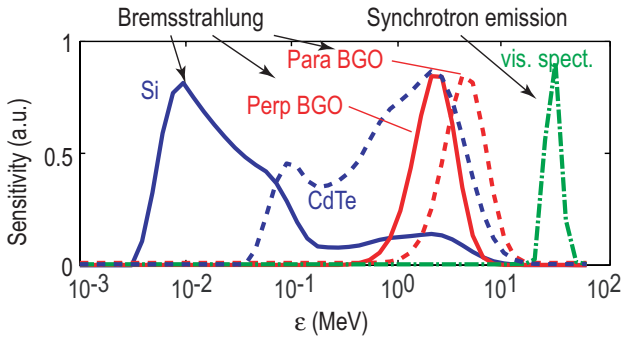

Figure 11. Sensitivity of different detectors on DIII-D to signals generated by different fast electron energies.

distribution function (obtained later), so e.g. synchrotron emission sensitivity actually rises monotonically with ε, but cuts off at high ε in figure 11 because the number of fast electrons drops off. Emission from electrons in the relativistic regime $\varepsilon > 1\,\mathrm{MeV}$ is directional, giving different sensitivity ranges for detectors placed perpendicular (above or below) or parallel to the RE beam (in the outer midplane). Sensitivities in figure 11 are given as a function of electron energy (not photon energy), so for example, $\varepsilon \approx 1\,\mathrm{MeV}$ electrons are predicted to give the greatest contribution to the CdTe detectors under these conditions, even though these detectors have a peak photon sensitivity around 100 keV. One concern is that SXR line emission (Ar Kα, 3.6 keV) will confuse interpretation of the Si SXR detectors. At the moment, SXR spectra are not available on DIII-D to check this. However, data taken with and without different foil high-pass filters (>10 keV and >20 keV) during the same RE plateau with the CdTe detectors revealed very little difference in received signal, suggesting that Ar Kα is not dominant over bremsstrahlung in terms of total brightness in the 2–10 keV range. Another concern is that different continua, e.g. thermal emission from hot graphite dust or bremsstrahlung, will confuse the synchrotron continuum interpretation. Forward and backward viewing spectrometers and cameras were used to verify that the measured continuum is indeed forward beamed and consistently rises in intensity towards the IR, consistent with synchrotron emission [22].

An example of a single-energy fit to the measured visible synchrotron emission spectrum is shown in figure 12. Using fits to synchrotron emission plus single-energy estimates of x-ray intensity, a rough $f_{\mathrm{RE}}(\varepsilon)$ can be reconstructed, as shown by the circles and error bars in figure 13. A more rigorous $f_{\mathrm{RE}}(\varepsilon)$ can be obtained by doing a simultaneous self-consistent fit to all the diagnostics, shown by the red curve in figure 13. Expected x-ray intensities are calculated using the bremsstrahlung simulations of [19] parametrized analytically as done in the GEANT4 code [20], while expected synchrotron emission is obtained from an analytical expression [21]. The dashed blue curve in figure 13 shows $\varepsilon f_{\mathrm{RE}}(\varepsilon)$, indicating that most of the kinetic energy in the RE beam is carried by electrons in the 1–5 MeV range. Trapped particles are neglected here—these are not expected to have any effect on the lower energy ($\varepsilon < 1\,\mathrm{MeV}$) portion of this analysis, but could add some small error (of order the trapping fraction) to interpretation of the relativistic, forward-beamed portion ($\varepsilon > 1\,\mathrm{MeV}$) of the energy distribution. Ignoring

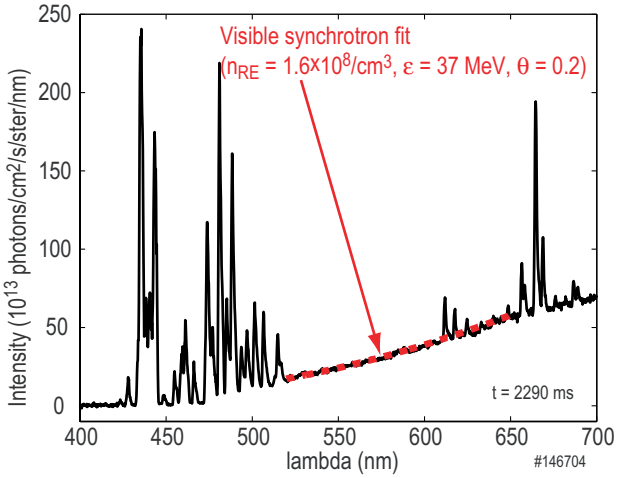

Figure 12. Measured visible survey spectrum looking tangentially into RE beam showing synchrotron continuum and (dashed curve) single-energy fit to continuum.

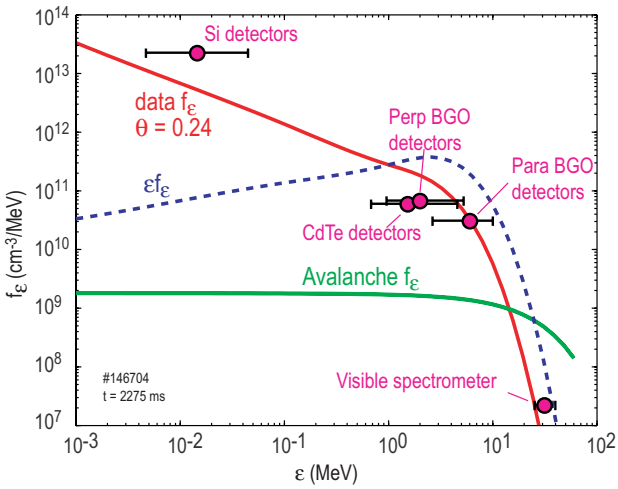

Figure 13. Reconstructed RE energy distribution function based on single-energy fits (points) as well as self-consistent fit to all detectors (red curve). Distribution function expected from avalanche model is shown by green curve.

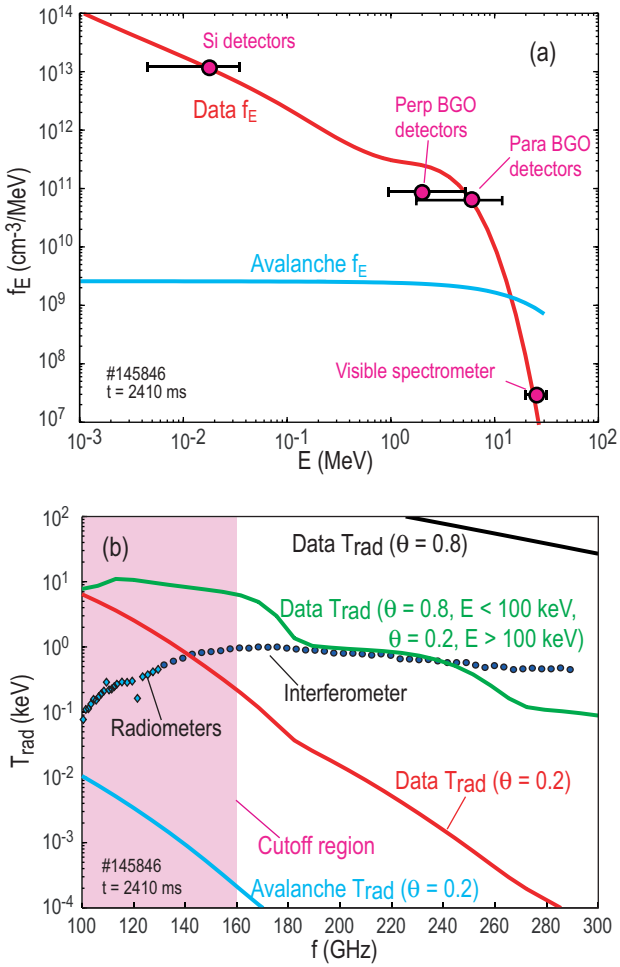

Figure 14. Estimates of RE energy/pitch angle distribution from: (*a*) bremsstrahlung and visible synchrotron emission; and (*b*) fits to ECE emission spectrum using fit distribution function $f_{\mathrm{RE}}(\varepsilon)$ from (*a*) but with different assumptions on pitch angle θ.

any anomalous loss, electrons with approximate energies $\varepsilon > 100\,\mathrm{keV}$ can be considered runaways in figure 13, in the sense that the collisional drag force is expected to be less than the parallel electric field force.

In the fit to $f_{\mathrm{RE}}(\varepsilon)$ in figure 13, a single pitch angle θ is assumed and varied to give the best fit to the data. The diagnostics at higher energy (HXR and synchrotron emission) are extremely sensitive to the RE pitch angle θ, but the SXR intensity is not, so this data is insensitive to θ at low energies. Typically, values of order $\theta \approx 0.2$ ($\approx 10^{\circ}$) are obtained. This is consistent with fits to the ellipticity of fast camera images of the RE visible synchrotron emission spot, which gave $\theta \approx 0.2$ [22]; this method of estimating θ is also dominantly sensitive to high-energy electrons.

The solid green curve in figure 13 is the distribution function expected from avalanche theory, $f_{\mathrm{RE}}(p) \sim \exp(-p/m_e c\bar{p})$, with $p \equiv m_e c\beta\gamma$ and $\bar{p} \equiv [3(Z+5)/\pi]^{1/2} \times \ln[\Lambda(Z)] \approx 46$ for argon [23]; the normalization is obtained from the plasma current, assuming all plasma current is carried by the fast electrons. This form is identical to the high-energy approximation of the avalanche distribution function suggested in [24] in the limit of large aspect ratio. In principle, avalanche theory should be valid here, since avalanche gain is expected to be significantly larger than RE seed formation throughout the CQ and RE plateau. Transport losses (ripple, drift orbit, etc) are not included in the avalanche theory curve. It can be seen that the measured distribution function appears skewed towards low energies relative to avalanche theory, possibly indicating an anomalous collisional drag on the fast electrons. Integrating over $\int \mathrm{d}\varepsilon\, f_{\mathrm{RE}}(\varepsilon) v$ in figure 13 and multiplying by RE beam cross section area gives a plasma current that is significantly larger than measured, suggesting that the distribution function is not uni-directional, i.e. there are REs are going in both directions (due to scattering, trapping, etc).

The electron cyclotron emission (ECE) spectrum indicates that mean RE pitch angle θ becomes larger at lower energies during the RE plateau. The measured RE ECE spectrum from ECE radiometers and a Michelson interferometer is shown by points in figure 14(*b*). Figure 14(*a*) shows the fit to $f_{\mathrm{RE}}(\varepsilon)$ using bremsstrahlung and synchrotron intensities (as done for a different shot in figure 13), then the same $f_{\mathrm{RE}}(\varepsilon)$ is used but

with different assumptions for θ to fit to the ECE spectrum in figure 14(b). The curves in figure 14(b) are predicted spectra for different assumptions of the pitch angle θ. It can be seen that the data is qualitatively fit using the measured distribution function $f_{\mathrm{RE}}(\varepsilon)$ and assuming a large pitch angle $\theta = 0.8$ for energies $\varepsilon < 100\,\mathrm{keV}$ and small pitch angle $\theta = 0.2$ for energies $\varepsilon > 100\,\mathrm{keV}$, supporting an increasing pitch angle towards lower RE energies. Fits assuming a constant pitch angle θ as a function of energy give much poorer matches to the data. The model curves in figure 14(b) are calculated using the Schott–Trubnikov formula for single particle x-mode ECE [25]. Collective effects are ignored, so these curves are not expected to be valid in the lower frequency cutoff region shaded in figure 14(b).

3.5. Current dissipation of RE plateaus with low Ar content

The decay of RE current seen in these experiments is qualitatively in agreement with avalanche theory with the addition of an anomalous loss term. According to avalanche theory, the growth of RE current can be described by $\nu_{\mathrm{R}} = C(E - E_{\mathrm{crit}})$, where $\nu_{\mathrm{R}} = J_{\mathrm{RE}}^{-1}\,\mathrm{d}J_{\mathrm{RE}}/\mathrm{d}t$ is the rate of change of RE current. In this equation, E is the toroidal electric field, C is essentially constant, and $E_{\mathrm{crit}} \propto n_{\mathrm{e,tot}}$ is the critical field for RE suppression [24]. Later experiments and calculations indicated that the equation $\nu_{\mathrm{R}} = C(E - E_{\mathrm{crit}})$ may also be valid for $E < E_{\mathrm{crit}}$, provided the rate of RE current decay is sufficiently slow [14]. Comparison with this equation is done for two data sets: ohmic coil ('E-coil') ramp experiments where the toroidal electric field is ramped up or down by the E-coil (described in this section); and MGI experiments (described in section 4) where the E-coil is used in current feedback mode (attempting to maintain the RE current constant) but a large quantity of impurities is injected into the RE beam. In both cases, the RE beam is created by small Ar pellet injection. In the E-coil ramp experiments, the magnitude of E tends to be large compared with $E_{\mathrm{crit}} \approx 0.1\,\mathrm{V\,m^{-1}}$, while in the MGI experiments, E and E_{crit} are often comparable in magnitude.

The toroidal electric field E on centre of the RE beam is estimated from the time evolution of the magnetic flux from JFIT, averaged over the RE beam radius. Obtaining E accurately inside the RE beam is challenging, as E is only measured directly by toroidal loops outside the vacuum vessel. During periods of changing RE current profile and position, E inside and outside the conducting wall are expected to be different. Additionally, estimates of the radial profile of E from avalanche theory indicate that E in the centre of the RE beam can be different from E outside the RE beam [14]. Differences between various methods of estimating E inside the RE beam are illustrated in figure 15, which shows time traces from a RE beam. At time $t = 2250\,\mathrm{ms}$, the E-coil ramp maintaining the RE current is stopped, resulting in a drop in toroidal loop voltage V_{loop} and an inward radial drift of the RE beam. Additionally, there are three large instabilities in the RE beam during the time window shown, two of which (at $t = 2224\,\mathrm{ms}$ and $t = 2258\,\mathrm{ms}$) are large enough to cause noticeable drops in plasma current. Figure 15(g) shows V_{loop} from JFIT (red curve), from the external measurement (green curve) and from the external measurement with the correction from avalanche theory. It can be seen that the JFIT V_{loop} is most

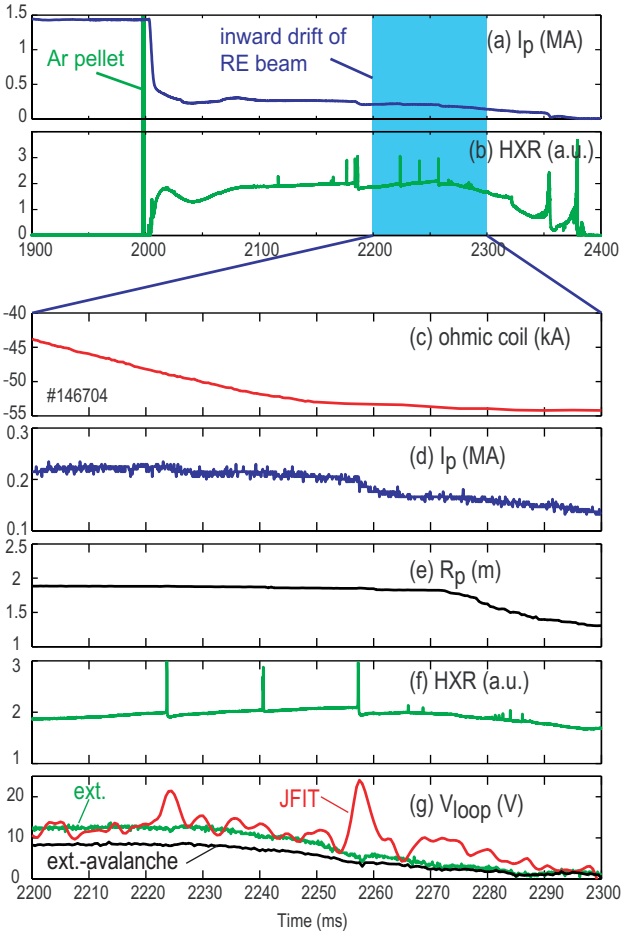

Figure 15. Time traces comparing different methods of estimating toroidal loop voltage in RE beam during in'drift of beam showing (broad time scale): (a) plasma current, (b) HXR signals; and (narrower time scale): (c) ohmic coil current, (d) plasma current, (e) radial position, (f) HXR signals and (g) loop voltage.

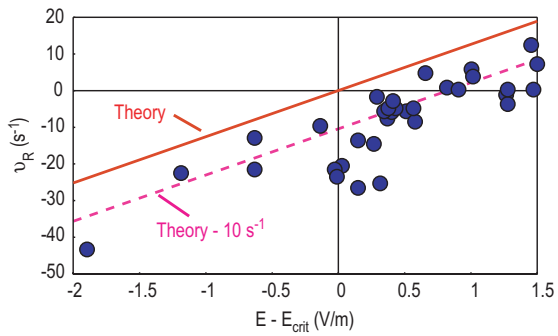

Figure 16. Measured RE current growth rate as a function of toroidal electric field $E - E_{\mathrm{crit}}$. Red line shows avalanche theory value. Dashed line shows theory value with added offset of $10\,\mathrm{s^{-1}}$.

responsive to the changes in plasma current and radial position, showing the expected rises in V_{loop} when the current is lost suddenly during instabilities or when the current channel drifts inwards. We therefore use the JFIT method for calculating V_{loop}, as the experiments discussed here are rarely fully steady state, with some motion and contraction of the RE current channel typical even in the middle of the RE plateau.

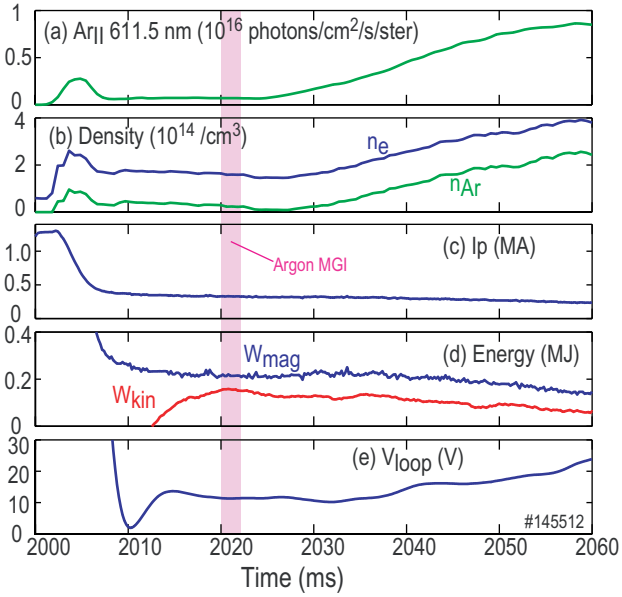

Figure 17. Time traces of a shot with Ar MGI at $t = 2020$ ms, showing (a) Ar II brightness, (b) electron and Ar^+ density, (c) plasma current, (d) RE beam energy and (e) loop voltage.

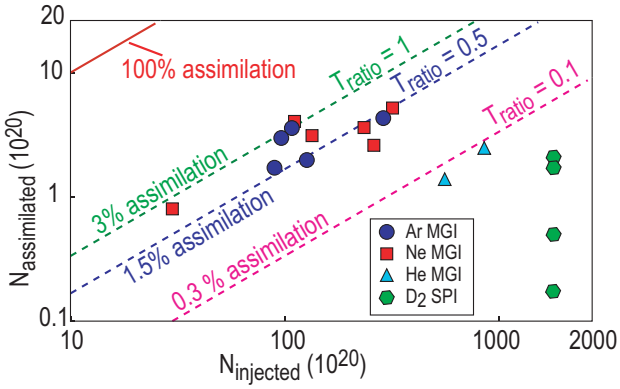

Figure 18. Assimilation of particles injected into RE plateau showing number of particles assimilated into RE beam versus number of particles injected.

Points in figure 16 show RE current growth rate ν_R as a function of $E - E_{crit}$ for E-coil ramp experiments (with the comparison taken in the middle of the RE plateau). For each data point, E is calculated from JFIT as described above, with a beam radius $a = 0.2$ m assumed for the current channel (the beam-averaged value of E is found to depend only weakly on the exact value taken for the beam radius). Due to the large number of data points, the argon fraction is not calculated carefully spectroscopically, as was done in select cases (e.g. figure 8); instead a typical Ar concentration of 10% is assumed in each case. Since the magnitude of $E_{crit} \approx 0.1\,\mathrm{V\,m^{-1}}$ tends to be small in these experiments, the exact Ar concentration is not important for figure 16. It can be seen that the data tends to lie $10\,\mathrm{s^{-1}}$ lower than expected from avalanche theory. This is consistent with previous analysis of the same data, which used the externally measured V_{loop} and avalanche correction to estimate the internal electric field [14]. In figure 16, it was attempted to use data from well-centred RE plateaus; as will be discussed in section 4.1, the anomalous loss term increases as the RE plateau is pushed into the wall.

4. Dissipation of RE plateau using massive particle injection

As shown in figure 3(b), injection of sufficient quantity of high-Z gas into RE beams causes an enhanced decay rate of the RE current. Time traces showing the time evolution of high-Z gas injection into a RE beam are shown in figure 17. At $t = 2020$ ms, MGI ($\sim$1000 $\mathrm{Torr^{-1}}$ of Ar) is fired into a RE plateau, creating a RE channel with majority (>50%) Ar^+ content. Figure 17(a) shows Ar II line brightness versus time, while figure 17(b) shows central electron and Ar^+ densities (neutral Ar is neglected; as described in section 3.3, it is believed that most argon in the core of the RE plateau is in singly ionized form). Figures 17(c) and (e) show plasma current and loop voltage respectively. It can be seen that, as the argon is assimilated into the RE beam, enhanced current decay occurs, even though there is an attempt by the plasma control system to maintain the current constant by raising the loop voltage. Figure 17(d) shows the RE beam energy versus time (magnetic W_{mag} and kinetic W_{kin}): W_{mag} is estimated from the JFIT magnetic reconstructions and W_{kin} is estimated from the diamagnetic loop signals [26]. Both methods are extremely approximate, since JFIT cannot reconstruct the plasma current profile accurately and the diamagnetic signals are very small and noisy during the RE plateau. Overall, however, the data suggests that $W_{mag} > W_{kin}$ and that both tend to decrease following massive argon injection.

Equilibrium assimilation of atoms injected either as gas (MGI) or large frozen pellets (shattered pellet injection, SPI) into RE beams appears to be fairly low, of order several per cent or less. This is shown in figure 18, where the number of particles assimilated into the RE plateau is shown as a function of the number of particles injected. Dashed lines give assimilation fractions estimated from pressure balance between ions and neutrals. Radial pressure balance of neutrals gives an expected assimilation fraction $f_{Assim} \approx (V_{beam}/V_{vac})(T_N/T_i)$, where $(V_{beam}/V_{vac}) \approx 1/30$ is the beam/vacuum chamber volume ratio, and $T_{ratio} = (T_N/T_i) \approx 1/2$ is the neutral/ion temperature ratio. The high-Z injection data appears consistent with the temperature ratio $T_{ratio} \approx 1/2$ measured for equilibrium (no MGI) RE beams, however, the lower assimilation of low-Z atoms appears more consistent with a lower temperature ratio $T_{ratio} \approx 1/10$. Pressure balance can be expected to be valid here since, unlike normal tokamak neutrals, the neutrals in the RE plateau undergo many momentum scattering collisions for every ionizing collision. For neutral argon, for example, we estimate an ionization rate (due to electron impact, including relativistic electrons) of order $\nu_{ion} \approx 200\,\mathrm{s^{-1}}$ and a momentum scattering rate with D^+ and/or Ar^+ of order $\nu_{mom} \approx 2 \times 10^4\,\mathrm{s^{-1}}$, so argon neutrals attempting to enter the RE beam experience many collisions with ions prior to being ionized [14]. The neutral pressure is not expected to be an important term in the RE current equilibrium: the argon ion gyrofrequency $\Omega_i \approx 4 \times 10^5\,\mathrm{s^{-1}}$ is large compared with the Ar^+ momentum scattering rate off Ar neutrals $\nu_{mom} \approx 8 \times 10^3\,\mathrm{s^{-1}}$, so ions are still confined radially

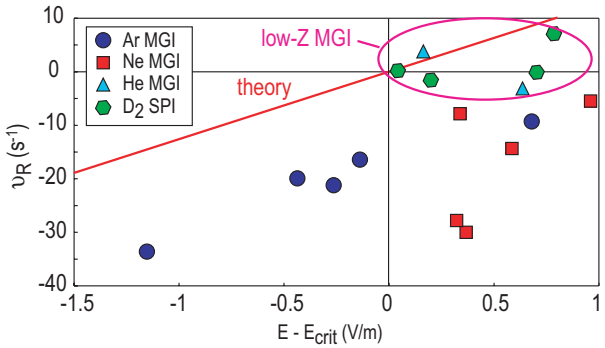

Figure 19. Measured RE current growth rate as a function of electric field following massive particle injection into RE beam.

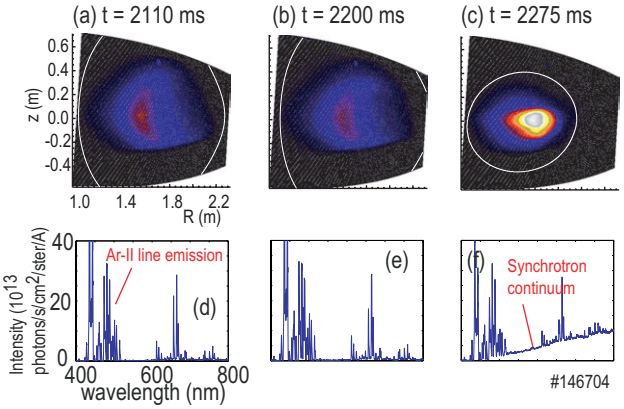

Figure 20. (*a*)–(*c*) images of visible synchrotron emission; and (*d*)–(*f*) survey spectra at same three time steps as RE beam moves into centre post.

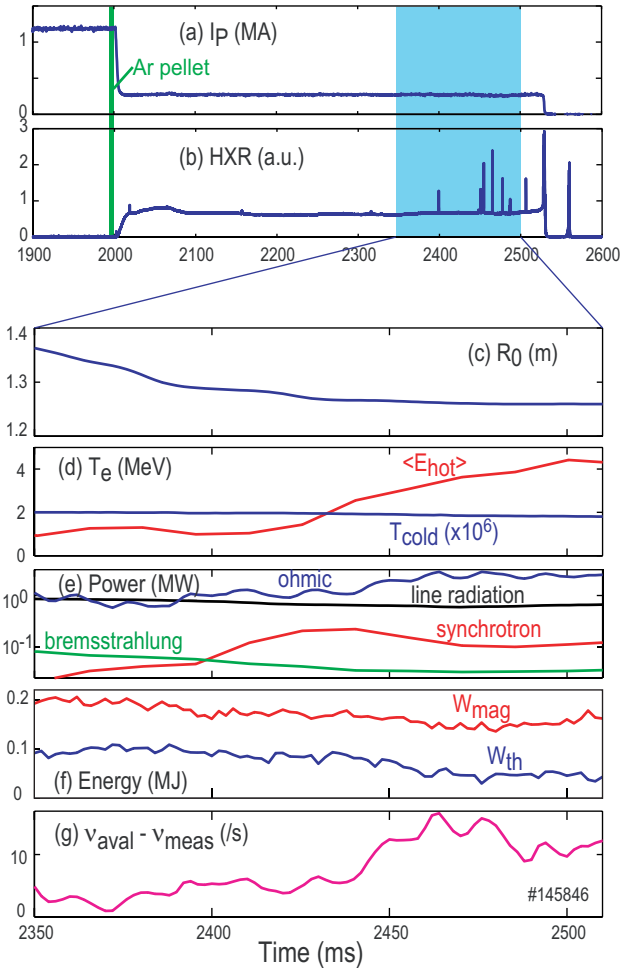

Figure 21. Time traces of RE beam moving into centre post showing (*a*) plasma current and (*b*) HXR signals; and smaller time window of: (*c*) radial position, (*d*) hot and cold electron temperatures, (*e*) input and output power, (*f*) beam energy, and (*g*) anomalous current loss rate.

by the magnetic field and we expect that plasma pressure is still balanced radially by $J \times B$, as in a conventional plasma.

Measured RE current growth rate following massive particle injection is shown in figure 19 as a function of beam-averaged toroidal electric field. In this data, the comparison between current growth rate and electric field is taken as late as possible in the RE plateau (before the final RE loss) to allow as much time as possible for toroidal symmetrization of the injected impurities. Toroidal symmetry is an issue because the ion temperatures are cold, so toroidal symmetrization times of order 10 ms or more are expected, while toroidal symmetry is assumed in the analysis. It can be seen that RE current decays much faster than expected by avalanche theory following high-Z particle injection, with loss rates as much as 30 s^{-1} below theory. On the other hand, low-Z particle injection results in a RE plateau which decays at a rate only slightly (perhaps 5 s^{-1}) below theory, as emphasized by the circle in figure 19. This result therefore suggests that the anomalous loss of RE current is caused by the presence of high-Z ions in the RE beam (even small concentrations, such as shown in figure 17) and that massive low-Z particle injection serves to dilute these ions, removing them from the core.

4.1. Evidence for radial transport loss of RE current

At present, the source of the observed anomalous loss of RE current is not certain. Likely loss channels are thought to be diffusion of REs into the chamber walls or anomalous drag by the cold background plasma, resulting in conversion of RE magnetic energy into line radiation. Present data seems to favour the first interpretation; this can be seen by an increase in anomalous loss rate despite a decrease in line radiation as RE beams are allowed to slowly drift into the centre post. An example of such a shot is shown in figure 20, where panels (*a*)–(*c*) show visible camera images of synchrotron emission at three different time steps as a RE beam moves into the centre post. Panes (*d*)–(*f*) show survey spectra at the corresponding time steps. The white lines in panels (*a*)–(*c*) correspond to the last closed flux surface from magnetic reconstructions. The sudden transition from crescent shaped to oval shaped synchrotron emission is not understood yet and is not pursued here. As the RE beam moves into the centre post, it can be seen that the RE beam shrinks and synchrotron emission increases—this increase could indicate more REs at higher energy or increased pitch angle. At the same time, there is a slight decrease in Ar II line emission, indicating a decreased coupling between fast and cold electrons, presumably due to increased fast electron energy.

Time traces with more detailed analysis of a similar shot (where the RE beam is allowed to drift into the centre post)

are shown in figure 21. Figure 21(*c*) shows the RE beam radial position, showing the inward drift of the RE beam after the E-coil ramp to sustain RE current is turned off. Figure 21(*d*) shows the mean fast electron energy $\langle E_{\rm hot}\rangle$ as well as the cold electron temperature $T_{\rm cold}$. It can be seen that the fast electrons heat as the plasma moves into the centre post, but the cold electrons cool, indicating a decreasing coupling between the (already only weakly coupled) fast and cold electrons. Figure 21(*e*) shows data on power input and output into the RE beam. Total ohmic power put into the beam is estimated from the central loop voltage from JFIT times the plasma current. Total radiated power is estimated from a foil bolometer array. IR synchrotron radiated power and total x-ray bremsstrahlung radiated powers are estimated from the energy distribution function. It can be seen that in the initial RE beam, ohmic input power is roughly balanced by line radiation. However, as the RE beam moves into the centre post, line radiation decreases, but ohmic input power increases, leading to an apparent power imbalance. Beam energy, figure 21(*f*), appears to be decreasing, so the missing power does not appear to be going into increasing the stored beam energy. As the beam moves towards the centre post, the anomalous current loss rate is seen to increase, from about $5\,{\rm s}^{-1}$, to greater than $10\,{\rm s}^{-1}$. Overall, this data is consistent with an anomalous loss due to diffusion of REs into the vessel wall. The missing energy loss rate of approximately $(1\,{\rm MW}/0.2\,{\rm MJ}) \approx 5\,{\rm s}^{-1}$ is comparable with the observed anomalous current loss rate of about $10\,{\rm s}^{-1}$. An anomalous increased dissipation of energy into the cold background plasma does not seem consistent with the data, since line radiated power decreases as the anomalous loss rate increases. Comparably detailed data for outward RE beam loss is not available at present.

5. Magnetic energy balance during RE final loss

Estimates of RE beam magnetic and kinetic energy in DIII-D suggest that, typically, $W_{\rm mag} > W_{\rm kin}$ as shown in figure 21. In ITER, with larger plasma current, it is thought that this ordering will be even more pronounced, since, roughly speaking, $W_{\rm kin} \propto I_{\rm RE}$ but $W_{\rm mag} \propto I_{\rm RE}^2$. The possible conversion of magnetic to kinetic energy during the RE final strike is therefore a significant concern for ITER. The present upper bound of 2 MA set for an ITER RE-wall final strike assumes 40% conversion of magnetic to kinetic energy [9]; this is based on observations in JET [11].

During the RE final loss, the RE beam current can be converted to wall current, converted to ohmic current, or be used to increase the beam kinetic energy. The first two loss channels can be seen in a detail of the final loss time traces, figure 22. When the RE beam strikes the wall, a roughly linear scrape-off of current is typically observed, figure 22(*a*). Multiple large HXR spikes are seen over some duration $\Delta t_{\rm HXR}$, indicating rapid loss of RE kinetic energy into the wall, possibly enhanced by some sort of instability. A rise in toroidal wall current $I_{\rm wall}$ is seen during this time, figure 22(*b*), indicating some conversion of RE current into wall current. After HXR signals have gone to zero, indicating a complete loss of REs to the wall, the remaining plasma current $I_{\rm ohmic}$ decays approximately exponentially on a timescale of

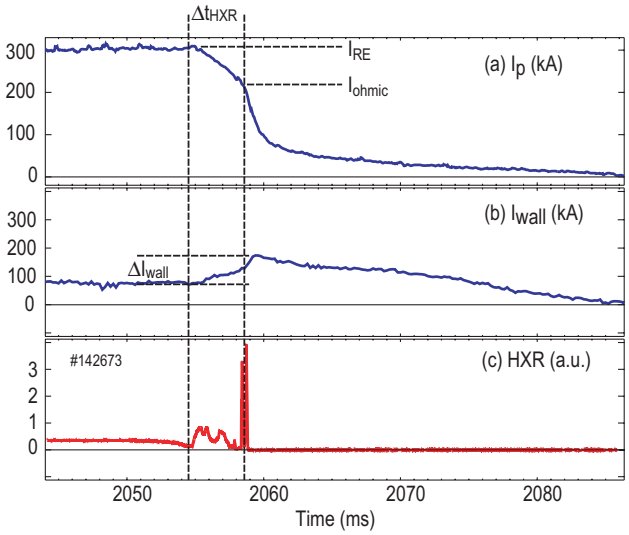

Figure 22. Time traces of RE final loss showing (*a*) plasma current, (*b*) toroidal wall current and (*c*) HXR signals.

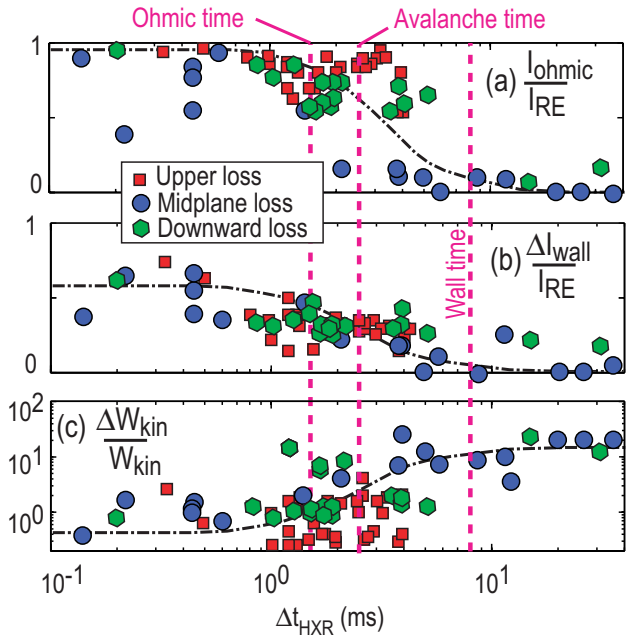

Figure 23. Data on final loss of RE current as a function of kinetic energy loss duration $\Delta t_{\rm HXR}$ showing (*a*) normalized ohmic current, (*b*) normalized gain in wall current, and (*c*) normalized kinetic energy deposited into wall. Dashed curves are smooth fits to data.

order $\tau_{\rm ohmic} \approx 1$–$2$ ms, consistent with ohmic current decay of a cold ($T_{\rm e} \approx$ several eV) ohmic plasma.

The amount of RE current converted into ohmic current is found to depend on the timescale of the final loss, as shown in figure 23(*a*), where $I_{\rm ohmic}/I_{\rm RE}$, ohmic current normalized to initial (at start of final loss) runaway current, is plotted as a function of $\Delta t_{\rm HXR}$. Each point corresponds to a different shot with upward, midplane (inward) and downward loss cases marked separately. It can be seen that shots with very rapid loss, $\Delta t_{\rm HXR} < \tau_{\rm ohmic}$ tend to have nearly complete conversion of RE current into ohmic current, consistent with present modelling work in progress and observations in JET [11]. Faster RE loss also appears to result in greater conversion of

RE current into wall current; this is shown in figure 23(*b*), where $\Delta I_{\rm wall}/I_{\rm RE}$, increase in wall current normalized to initial runaway current, is plotted.

As most RE current is converted to ohmic current in fast final RE loss cases, we expect that less magnetic energy is available for conversion to kinetic energy. This is qualitatively observed in figure 23(*c*), where, an estimate of the amount of kinetic energy deposited into the wall, normalized by initial RE beam kinetic energy, is plotted. As discussed above, estimating the kinetic energy in the RE beam is challenging because diamagnetic loop signals are small and noisy; additionally, the measured energy distribution such as figure 13 covers many orders of magnitude so direct integration of the measured energy distribution also results in a very large scatter in the estimated values of kinetic energy for different shots and time steps. To obtain a qualitative estimate of $\Delta W_{\rm kin}/W_{\rm kin}$, we therefore integrate the HXR signal over the final loss and normalize in each shot to $I_{\rm RE}$ (which is expected to be roughly proportional to $W_{\rm kin}$). Finally, the data points from each direction (upper, midplane, and downward loss) are normalized separately so that the first several points (with fastest $\Delta t_{\rm HXR}$) in each group give $\Delta W_{\rm kin}/W_{\rm kin} \approx 1$ as expected from the results of figure 23(*a*). For the integral over HXR signals, a toroidal average of detectors is used to minimize possible pointing variation of the forward-beamed HXR signals. Also, detectors poloidally farthest from the strike location are used (upper detectors for downward loss and lower detectors for upward or midplane loss), again to minimize scatter in signal from shot-shot variations in RE beam strike location during the final loss. An inconsistency revealed by this analysis is that kinetic energy increases of up to $\Delta W_{\rm kin}/W_{\rm kin} \approx 20$ are obtained from the HXR data of figure 23(*c*), suggesting an initial magnetic/kinetic energy ratio $W_{\rm mag}/W_{\rm kin} \approx 20$; while magnetics data such as figure 16(*e*) suggests an initial (pre-final loss) ratio $W_{\rm mag}/W_{\rm kin} \approx 2$. The source of this inconsistency has not been identified, but may be due to the large uncertainties in interpretation of the HXR data. For example, we are simply integrating over HXR signals here when comparing different shots, but the energy evolution of slow and fast final loss events could be quite different, resulting in different interpretations of HXR signal levels. The details of how the RE kinetic energy is deposited into the graphite walls of DIII-D is not well understood at present. No clear post-operation damage has been observed in the vessel tiles from RE-wall strikes, suggesting that perhaps the kinetic energy is deposited deeply in the graphite tiles.

6. Summary

The measurements presented here should help guide future experiments and modelling towards the goal of designing an effective disruption mitigation system (DMS) with RE dissipation for ITER. We have shown that the RE plateau in DIII-D forms a fairly narrow ($a \approx 0.3$ m) beam of current-carrying hot ($\varepsilon > 1$ keV) electrons inside a larger ($a > 0.5$ m) dense plasma of cold ($T_{\rm e} \approx$ 1–2 eV) electrons. Impurities in the RE beam are shown to be mostly singly charged ions, with neutrals largely excluded from the RE beam centre. Assimilation of additional impurities injected into the RE beam is shown to proceed on a slow (~30 ms) timescale to an equilibrium reasonably well described by pressure balance between hotter core ions and colder outer neutrals. For typical DIII-D RE plateaus with a minority (~10%) argon content, the RE energy distribution function is shown to be quite broad and more skewed to lower energies than expected from avalanche theory. Dissipation of RE current in these plateaus appears to be faster than predicted by avalanche theory, by of order $10\,{\rm s}^{-1}$; present data suggests that this anomalous loss is an enhanced radial diffusion of REs into the wall caused by the presence of high-Z ions in the RE beam, possibly via pitch-angle scattering. The final loss of RE beams to the wall is shown to convert very little magnetic energy into kinetic energy in cases where the RE beam moves into the wall on a time scale shorter than the ohmic decay time scale of order 1–2 ms.

Overall, the results presented here seem encouraging for ITER RE plateau dissipation. Vertical instability (VDE) time scales in ITER are expected to be of order 500 ms (but could be lower for high initial vertical displacements). Assuming a diffusive assimilation of impurities, expected argon or neon assimilation time scales into a RE plateau in ITER might be expected to be of order 10 times longer than DIII-D, so perhaps 300 ms. It therefore seems reasonable to expect that massive neon or argon injection into the RE plateau could be performed quickly enough to help dissipate RE current before the final loss. Additionally, the data shown here indicates that conversion of magnetic energy to kinetic energy (and resulting first wall damage) in the RE final strike can be quite small in some cases, less than the 40% presently assumed for ITER. Future experiments and modelling will attempt to further understand the physics of the RE beam structure, dissipation, and loss for application to ITER.

Acknowledgments

This work was supported in part by the US Department of Energy under DE-FG02-07ER54917, DE-FG03-97ER54415, DE-FC02-04ER54698, DE-AC05-00OR22725, DE-AC52-07NS27344 and DE-AC05-06OR23100. Suggestions from R. Goldston are acknowledged.

Disclaimer

The views and opinions expressed herein do not necessarily reflect those of the ITER Organization.

References

[1] Nygren R. *et al* 1997 *J. Nucl. Mater.* **241** 522
[2] Hender T.C. *et al* 2007 Progress in the ITER physics basis: chapter 3. MHD stability, operational limits and disruptions *Nucl. Fusion* **47** S128–202
[3] Eriksson L.G. *et al* 2004 *Phys. Rev. Lett.* **92** 205004
[4] Izzo V.A. *et al* 2011 *Nucl. Fusion* **51** 063032
[5] Sokolov Yu. A. 1979 *JETP Lett.* **29** 218
[6] Sizyuk V. *et al* 2009 *Nucl. Fusion* **49** 095003
[7] Hollmann E.M. *et al* 2011 *J. Nucl. Mater.* **415** S27
[8] Konovalov S. *et al* 2010 Characterization of runaway electrons in ITER *Proc. 23rd Int. Conf. on Fusion Energy 2010 (Daejeon, South Korea, 2010)* (Vienna: IAEA) CD-ROM file ITR/P1-32 and www-pub.iaea.org/mtcd/meetings/PDFplus/2010/cn180/cn180_papers/itr_p1-32.pdf

[9] Sugihara M. *et al* 2012 Disruption impacts and their mitigation values *Proc. 25th Int. Conf. on Fusion Energy 2012 (San Diego, CA, 2012)* (Vienna: IAEA) CD-ROM file ITR/P1-14 and www-pub.iaea.org/MTCD/Meetings/PDFplus/2012/cn197/cn197_Programme.pdf
[10] Saint-Laurent F. *et al* 2009 Control of runaway electron beams on Tore Supra *36th EPS Conf. (Sofia, Bulgaria 2009)* http://epsppd.epfl.ch/Sofia/pdf/P4_205.pdf
[11] Loarte A. *et al* 2011 *Nucl. Fusion* **51** 073004
[12] Luxon J.L. 2002 *Nucl. Fusion* **42** 614
[13] Eidietis N.W. *et al* 2012 *Phys. Plasmas* **19** 056109
[14] Hollmann E.M. *et al* 2011 *Nucl. Fusion* **51** 103026
[15] Humphreys D.A. *et al* 2006 *Phys. Plasmas* **13** 056113
[16] James A.N. *et al* 2012 *Nucl. Fusion* **52** 013007
[17] Sommers H.P. *et al* 2002 *Plasma Phys. Control. Fusion* **44** B323
[18] Scott H.A. 2001 *J. Quant. Spectrosc. Radiat. Transfer* **71** 689
[19] Seltzer S.M. *et al* 1985 *Nucl. Instrum. Methods* **12** 95
[20] Agostinelli S. *et al* 2003 *Nucl. Instrum. Methods* **506** 250
[21] Pankratov I.M. 1999 *Plasma Phys. Rep.* **25** 145
[22] Yu J.H. *et al* 2013 *Phys. Plasmas* **20** 042113
[23] Parks P.B. *et al* 1999 *Phys. Plasmas* **6** 2523
[24] Rosenbluth M.N. and Pustniski S.V. 1997 *Nucl. Fusion* **37** 1355
[25] Celata C.M. *et al* 1977 *Nucl. Fusion* **17** 4
[26] Fujita T. *et al* 1991 *J. Phys. Soc. Japan* **60** 1237